Nano Research

Open Access

Research Article

Surface embedded binary Co-Cu hydroxy phosphate over surface of oxy/hydroxides for efficient nitrate reduction to ammonia

Chun Zhu, Yifei Yang, Yike Jing, Zhen Zeng, Xuesong Yi, Wei Sun ✉, and Fei Yang ✉

Key Laboratory of Agro-Forestry Environmental Processes and Ecological Regulation of Hainan Province, School of Environmental Science and Engineering, Hainan University, Haikou 570228, China

Cite this article: *Nano Research*, **2025**, *18*, 94907048. https://doi.org/10.26599/NR.2025.94907048

ABSTRACT: Electrochemical nitrate reduction reaction (NO_3RR) to ammonia is a promising approach to address excess N-contamination in aqueous environment but suffers from a limited ammonia yield and selectivity due to the low concentration and sluggish kinetics. This work reports a three-dimensional porous electrode with binary Co_2Cu_1 hydroxy phosphate embedded into the surface of Ni_3Co_1 oxy/hydroxides (CoCu-PH@NiCo/Ni, "PH" means phosphate-hydroxide), which delivers a yield of 4.13 $mg \cdot h^{-1} \cdot cm^{-2}$ with a high Faraday efficiency of 92.6% under a low nitrate concentration of 40 mM and provide an impressive stability. This embedded structure of the as-prepared catalyst exhibits unique metal coordination ligands and valence states different from the unitary hydroxy-phosphate. The electrochemical *in situ* infrared spectra and theoretical calculations revealed that the Co sites with the ability to dissociate water molecular to form adsorbed OH* can effectively provide the required protons for the deoxygenation and hydrogenation steps during NO_3^- conversion, thereby, effectively reducing the energy barrier of the key transition states in the NO_3RR process to improve the intrinsic kinetics. We demonstrate that the rational design of binary components with the appropriate ability to activate water molecules as well as the three-dimensional porous skeletal structure are expected to promote effectively the low-concentration nitrates conversion to ammonia.

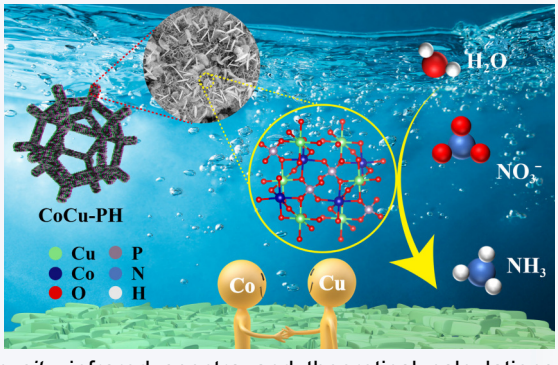

KEYWORDS: nitrate reduction, hydroxy phosphate, surface embedded, water dissociation, active hydroxy adsorbed

1 Introduction

The growing global population and the accompanying huge demand from industry and agriculture have led to severe nitrogen emissions, which have seriously threatened the global nitrogen cycle. Discharge of household sewage and industrial wastewater containing high concentrations of nitrates (NO_3^--N) results in eutrophication of natural waters, which is harmful to natural aquatic environments as well as potentially affecting human and mammalian health [1–3]. Recently, the electrochemical nitrate reduction reaction (NO_3RR) to ammonia (NH_3) has become a promising strategy for nitrate removal [4–7]. The NH_3 is not only the fertilizer industry's primary raw material but also an ideal intermediate for energy storage and a carbon-free energy carrier for renewable energy [8]. Thus, the NO_3RR route has the advantages of being eco-friendly, low-cost and producing valuable NH_3 compared to the conventional removal of nitrate from wastewater by biological denitrification, which aims at the conversion of nitrate to nitrogen gas [4, 9, 10]. It should be noted, however, that the actual nitrate concentration in the wastewater fluid is low and even when concentrated by membrane technology only reaches 10–100 mM, which is also an order of magnitude lower than that used electrolyte (often 1 M) in current NO_3RR studies. The low-concentration nitrate will inevitably limit the mass transfer at the electrode interface, thereby reducing the electroreduction polarization current [11, 12]. Moreover, competitive hydrogen evolution reaction (HER) will further reduce Faraday efficiency (FE) and increase the energy consumption of ammonia conversion since the NO_3RR involved a complex 8-electron reaction with sluggish kinetics [13, 14]. Therefore, the development of efficient NRR-catalysed electrodes for low-concentration nitrate electroreduction is crucial and still faces significant challenges.

To date, the most efficient catalysts for NO_3RR are the copper (Cu)-based materials due to their favorable ability to bind NO_3^- and high NH_3 conversion selectivity, such as Cu/Cu_2O [15, 16], Ru–Cu

Received: July 31, 2024; **Revised:** September 10, 2024
Accepted: September 23, 2024

✉Address correspondence to Wei Sun, weisun@hainanu.edu.cn; Fei Yang, fei.yang@hainanu.edu.cn

nanowires [17], CuFe bimetal [18], Cu clusters/TiO_{2-x} [19], BCN@Cu [20] and Rh@Cu [21] have been reported recently with high yield rate at high concentrations of NO_3^- (≥ 100 mM). Although Cu-based materials are regarded as potential candidates for replacing noble metal catalysts, they are inherently susceptible to deactivation during the long-term operation of cathode corrosion in alkaline environments [22]. restricted its application under low-concentration conditions. Heteroatom alloying or doping [22–25] and size-controlled nanostructure engineering [17, 19, 26, 27] are the most commonly used strategies for enhancing the overall performance of NO_3RR. Additionally, a non-oxide phase matrix has obvious advantages in improving electrode conductivity, especially metal phosphate [28–30], which widely used electrocatalyst for water splitting. Considering the formation of N–H (hydrogenation for adsorbed nitrogen) during the NO_3RR process, the appropriate addition of catalytic components that promote dissociated water molecules will help reduce the energy barrier for ammonia formation. The cobalt phosphates (often referred to as Co-Pi), first reported by the research of Kanan and Nocera [31], have inspired increasing attention [32, 33] due to the versatile coordination structures as a result of the presence of phosphate/pyrophosphate and crystal water ligands [34]. Regarding this, introducing Cu on the matrix of Co-Pi to form binary CoCu-Pi with dual active sites may improve the nitrate reduction performance and NH_3 selectivity at low concentrations. Over the past few decades, the three-dimensional (3D) structural configurations with interconnected porous channels have been verified to be the most effective strategies for improving the migration of low-concentration ions [35]. In addition, the percolation method allows the fluid to completely pass through the 3D porous skeleton, which can further enhance the proximity of nitrate ions to the vicinity of the electrode and overcome the adverse effects of the cathode-repelling anions [36].

Herein, a novel 3D architecture electrode is fabricated by a two-step method in which Ni-Co oxy/hydroxides ($Ni_3Co_1O_xH_y$) are firstly electrodeposited on a Ni foam substrate and follow hydrothermal growth of binary Co-Cu phosphate (CoCu-PH, "PH" means phosphate-hydroxide). The binary CoCu-PH is embedded into the sheet surface of $Ni_3Co_1O_xH_y$, which gives the overall morphology of the electrode shows an interlocking structure, thereby we denoted the electrode as CoCu-PH/NiCo@Ni. The X-ray adsorption and Raman spectra indicated that the binary sites over the active phase are coordinated by phosphate and oxy/hydroxyl instead of a single phosphate coordination. The multiple coordination enriches the active site's electronic structure and changes its valence states. The prepared CoCu-PH/NiCo@Ni exhibits remarkable NO_3RR activity before triggering HER and delivers a high NH_3 yield rate of 4.13 $mg \cdot h^{-1} \cdot cm^{-2}$ with the Faraday efficiency of 92.6% under a low concentration (NO_3^-, ~ 40 mM), which are much higher than a single phosphate (CoPi and CuPi). Electrolytic cells assembled with CoCu-PH/NiCo@Ni as cathode and $RuIrO_x$/Ti as anode can be operated under cyclic electrolysis for more than 100 h without loss of activity. The post-characterizations revealed that the morphological structure remains intact, but a composition reconstructed occurs because the phosphate is largely lost.

2 Results and discussions

2.1 Synthesis and characterizations of CoCu-PH/NiCo@Ni

Figure 1(a) simply schematizes the preparation process of the CoCu-PH/NiCo@Ni. Firstly, the pre-treated 3D porous Ni foam (Fig. S1 in the Electronic Supplementary Material (ESM)) served to support the electrodeposited binary Ni-Co oxy/hydroxides (Ni:Co = 3:1, $Ni_3Co_1O_xH_y$), to protect the Ni metal surfaces susceptible to corrosion and provide more attachment sites for the growth of subsequent catalytic phases. The CoCu-PH catalytic phase is grown on the surface of Ni-Co oxy/hydroxides by a hydrothermal process with common Co and Cu nitrates. Note that the substrate-intermediate layer-catalytic layer has the same element as each other to enhance the binding strength of the different layers and improve the stability of the whole electrode. The reason why we use nickel foam as the substrate of the catalyst is that it has high porosity, three-dimensional network structure, high specific surface area and good conductivity, which can promote the electrochemical reduction of NO_3^- [37]. This design concept is widely used in dimensional stable anode (DSA) electrodes [38], which can be operated stably for a long period in several important industrial scenarios. Besides, to prevent the size of solids from becoming too large result of the rapid Wald ripening, the macromolecular organic substance of polyvinylpyrrolidone (PVP, molecular weight ~ 4000) was added to the hydrothermal solution, which is expected to have a capping effect to prevent the particles from growing quickly. The morphology of electrodeposited $Ni_3Co_1O_xH_y$ is shown in Fig. 1(b), in which the sheet structure is found and presents a multilayered structure well covered on the metallic Ni foam (Fig. S2 in the ESM). Figures 1(c) and 1(d) show the morphology of prepared CoCu-PH/NiCo@Ni, it can be found that some large flakes of Co-Cu phosphate are embedded into the surface of $Ni_3Co_1O_xH_y$.

This embedded structure is also clearly observed in the performed transmission electron microscopy (TEM, Fig. 1(e)). A large amount of phosphate sheets fully interacts with the intermediate layer of $Ni_3Co_1O_xH_y$, rather than just covering the surface. High-resolution TEM (HRTEM) was employed to observe the micro surface structure, as shown in Figs. 1(f) and 1(g), which correspond to the marked regions 1 and 2 in Fig. 1(e). The localized lattice spacing in Fig. 1(f) is about 2.643 Å, which can be assigned to the (112) facet of the hydroxy phosphates ($Co_2(OH)PO_4$). Since the ionic radius of Co^{2+} (0.74 Å) and Cu^{2+} (0.73 Å) are relatively close to each other, the crystal spacing between the $Co_2(OH)PO_4$ and $Cu_2(OH)PO_4$ is also similar, which can be verified from X-ray diffraction (XRD) patterns (Fig. S3 in the ESM). In addition, there are amorphous areas and defect locations in some places (marked in Fig. 1(f)). These defects can provide active sites. The surface defects circled in the TEM image can be used as active sites for catalytic reactions. These active sites have unique electronic structures and geometric configurations [39]. They can adsorb and activate reactants, increase the number of active sites of the catalyst and promote the catalytic reaction. Appropriate defect structure can enhance the stability of the catalyst, prevent deactivation in the catalytic process, prolong the life of the catalyst and improve the importance of the catalyst's performance. The embedding structure is likewise clearly visible in Fig. 1(g), where the lattice fringe corresponds to the (110) facet of $NiCoO_xH_y$. Figure 1(h) is the high angle annular dark field (HAADF) image of CoCu-PH/NiCo@Ni, in which the binary CoCu-PH shows more brightness, indicating better electrical conductivity. Differences in elemental distributions can be distinguished from the mapping of the elements, where Co and Cu are more intensively distributed in the binary CoCu-PH fraction, as expected. The quantitative analysis of each element is shown in Fig. S4 in the ESM, where Co:Cu (atomic ratio) is slightly

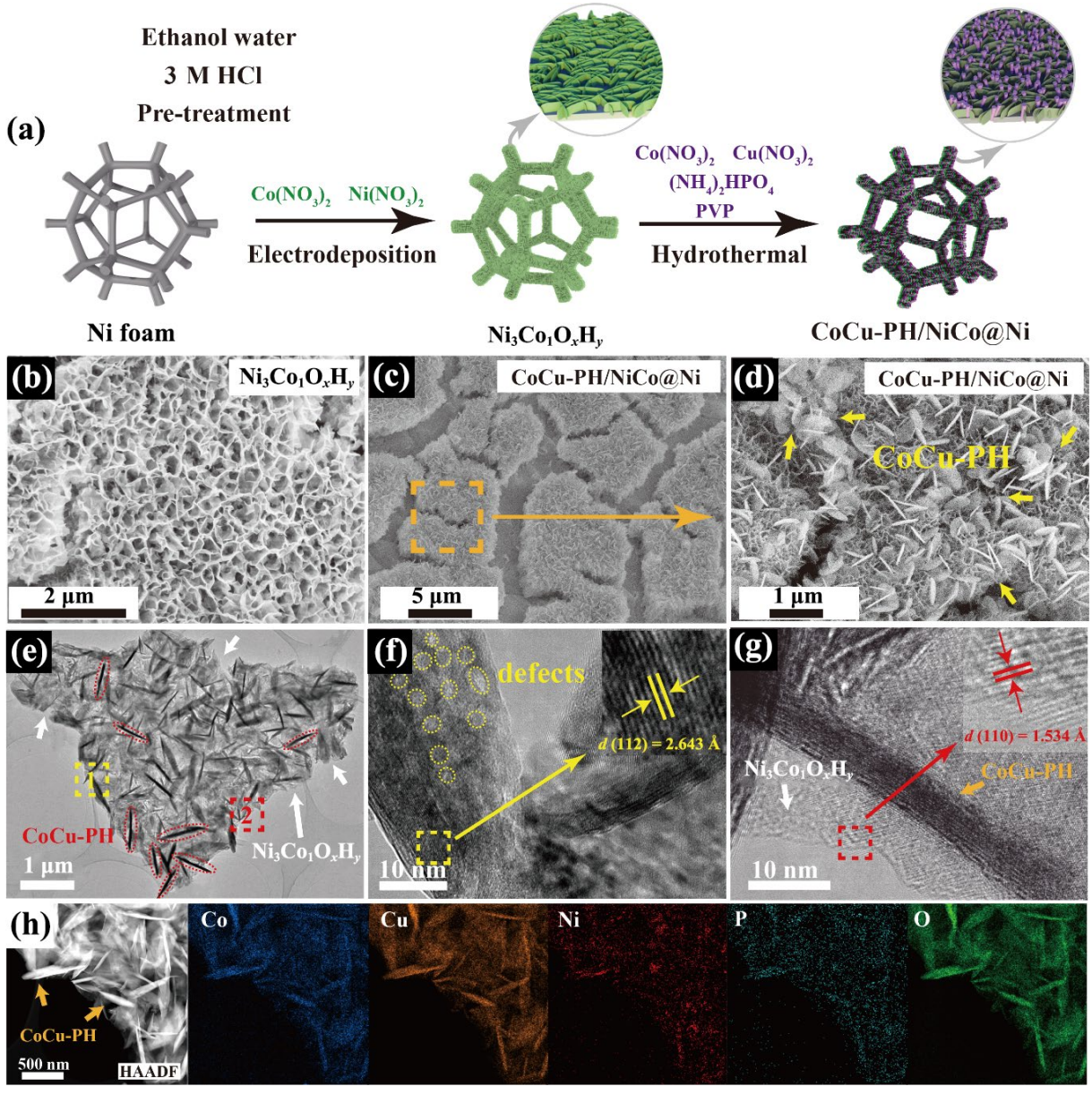

Figure 1 Preparation and characterizations of CoCu-PH@NiCo/Ni. (a) Schematic diagram of the preparation process. (b) SEM image of electrodeposited $Ni_3Co_1O_xH_y$. (c) SEM image of CoCu-PH@NiCo/Ni, (d) amplification of selected area in (c). (e) TEM image of CoCu-PH@NiCo/Ni. (f) and (g) HRTEM images corresponding to the selected area in (e). (h) HAADF image and elemental mapping images.

above 2.5:1, which is as expected because the intermediate layer contains a small amount of Co.

2.2 Structures and interfacial interaction of CoCu-PH/NiCo@Ni

This embedded structure will not only effectively improve the adhesion firmness of the catalyst, but also enrich the coordination structure of the active site. To investigate that, we first employed Raman to recognize the ligands over the CoCu-PH/NiCo@Ni and used the pure $Co_2(OH)PO_4$ and $Cu_2(OH)PO_4$ as the references. As shown in Fig. 2(a), it can be found that the strong peak located at ~ 970 cm^{-1} can be assigned to the contribution of the ligand of PO_4^{3-} and it is situated exactly between $Co_2(OH)PO_4$ and $Cu_2(OH)PO_4$. For the binary CoCu-PH, there is a very broad peak between 350–680 cm^{-1}, which may be due to the overlapping contribution of the corresponding Co–O/OH and Cu–O/OH ligands, as well as includes the intermediate layer of $Ni_3Co_1O_xH_y$, because the ligand of Ni–O/OH is also in this range [40].

The Raman can be used to understand the basic ligands of CoCu-PH/NiCo@Ni, but it is difficult to obtain its precise coordination structure, so the X-ray adsorption spectra (XAS) were performed. Figure 2(b) is the X-ray absorption near edge structure (XANES) of the Co-K edge of different Co-based materials, the pre-edge peak is stemmed from the transition of Co-1s→3d. The pre-edge peak intensity depends on the symmetry of the coordination structure, lowing the symmetry will increase the intensity [41]. The intensity of CoCu-PH is higher than that of $Co_2(OH)PO_4$, indicating that the incorporation of Cu may lower the coordination symmetry of CoO_6. The 1st of XANES is a useful way to identify the valence state of the central atom and a higher oxidation state typically leads to a higher energy of edge adsorption [42–44]. The insert of Fig. 2(b) compares the 1st spectra of CoCu-PH and $Co_2(OH)PO_4$, the

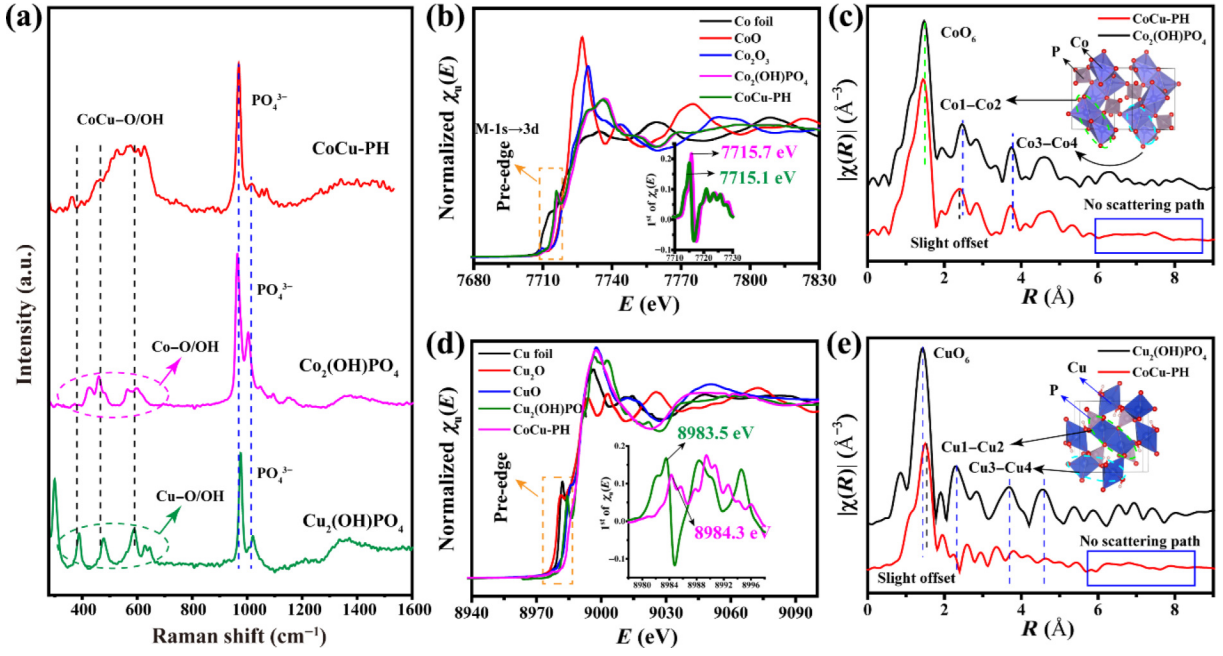

Figure 2 Structural and chemical states analysis of prepared catalyst. (a) Raman spectra of CoCu-PH@NiCo/Ni, $Co_2(OH)PO_4$ and $Cu_2(OH)PO_4$. (b) Co K-edge XANES spectra of different Co-based materials. The insert compares the 1st spectra of XANES of CoCu-PH and $Co_2(OH)PO_4$. (c) k^2-FTEXAFS spectra of Co K-edge for CoCu-PH and $Co_2(OH)PO_4$. (d). Cu K-edge XANES spectra of different Cu-based materials. The insert compares the 1st spectra of XANES of CoCu-PH and $Cu_2(OH)PO_4$. (e) k^2-FTEXAFS spectra of Cu K-edge for CoCu-PH and $Cu_2(OH)PO_4$. The k-range is set at 2–14 for both Co- and Cu-based materials.

absorption edge position of the former is 0.6 eV lower than that of the latter, indicating that the valence state of Co in CoCu-PH may be lower than 2+. Figure 2(c) corresponds to the k^2-weighted backward Fourier transforms of extended X-ray absorption fine structure (k^2-FTEXAFS), in which the length of Co1–Co2 coordination is slightly lower than that of $Co_2(OH)PO_4$. We speculate that it may be associated with the lower radius of Cu or that Cu itself has a Jahn–Teller distortion effect, both of these factors can act as a compression effect that causes the crystal structure to shrink appropriately [45, 46]. Besides, in the R range of 6–8 Å (R is radial distance), there are no scattering paths, which also represents the generation of defects or amorphous as amorphous or defect can effectively break the periodic ordered coordination.

Figures 2(d) and 2(e) are the Cu-K edge XANES and k^2-FTEXAFS. The 1st spectra clearly show that the valence state of Cu is higher in CoCu-PH compared to that of $Cu_2(OH)PO_4$, which is opposite the change in Co, demonstrating the existence of binary interactions in the CoCu-PH. In the k^2-FTEXAFS, the bond length of CuO_6 coordination is slightly higher than that of $Cu_2(OH)PO_4$, verifying the distortion of crystal structure in the binary CoCu-PH. We also noted the intensity of the scattering paths between Cu-Cu is substantially weakened, which may be related to the low content of Cu or its more disordered arrangement. The scattering paths are also very weak when $R > 6$ Å, which is the same as for Co-EXAFS.

2.3 The NO_3RR performance evaluation

Due to the alkaline medium being able to push back the onset potential of competitive HER, the NO_3RR performance of electrodes was evaluated under 0.1 M NaOH and by using a standard three-electrode system at room temperature (25 °C). Firstly, the NO_3RR performance of the prepared CoCu-PH/NiCo@Ni was investigated at different NO_3^- concentrations solutions, as shown in Fig. 3(a). In the non-nitrate medium, the activity of HER is weak and it exhibits significant polarization current only after −0.25 V vs. reversible hydrogen electrode (RHE). When added nitrate, there is a start of polarization current appearance at −0.05 V and a platform current density originated from diffusion-limited is achieved before −0.25 V, suggesting that CoCu-PH/NiCo@Ni can effectively promote NO_3RR before HER is triggered. More important, the diffusion-limited current density increases with the nitrate concentration and exhibits a good linear relationship (Fig. 3(b)). Notably, the half-wave potential independent of the nitrate concentration, indicates that the polarization current essentially derives from NO_3RR and the change in current depends on the concentration of nitrate and the mass transfer efficiency. Then, we compared the reduction performance of different materials in a mixed solution of 0.1 M NaOH and 80 mM NO_3^- (Fig. 3(c)), it can be found that the other materials did not show the platform current density of NO_3RR except for CoCu-PH/NiCo@Ni and Cu-PH/NiCo@Ni. We notice that the Cu-PH/NiCo@Ni has a lower onset potential (Fig. S5 in the ESM), verified that Cu-based materials have excellent nitrate to nitrite transfer activity, but its kinetics is not as high as that of CoCu-PH/NiCo@Ni (Fig. S6 in the ESM). The higher kinetics exhibit lower charge transfer resistance (R_{ct}), which can be verified by electrochemical impedance spectroscopy (EIS). As shown in Fig. S7 in the ESM, the R_{ct} of CoCu-PH/NiCo@Ni is only 4.63 Ω, which is lower than Cu-PH/NiCo@Ni (4.77 Ω) and much less than Co-PH/NiCo@Ni. Moreover, the Co-PH/NiCo@Ni has almost no NO_3RR activity, especially before −0.25 V and the highly active CoCu exhibits the smallest R_{ct} and the largest electrochemical active surface area (ECSA), which means that the rapid transfer kinetics and high abundance of active centers improve the activity of NO_3RR (Fig. S8 in the ESM). It is therefore reasonable to believe that the high activity of CoCu-PH/NiCo@Ni can be attributed to the synergistic catalytic effect of the binary Co and Cu.

To further access the NO_3RR performance of CoCu-

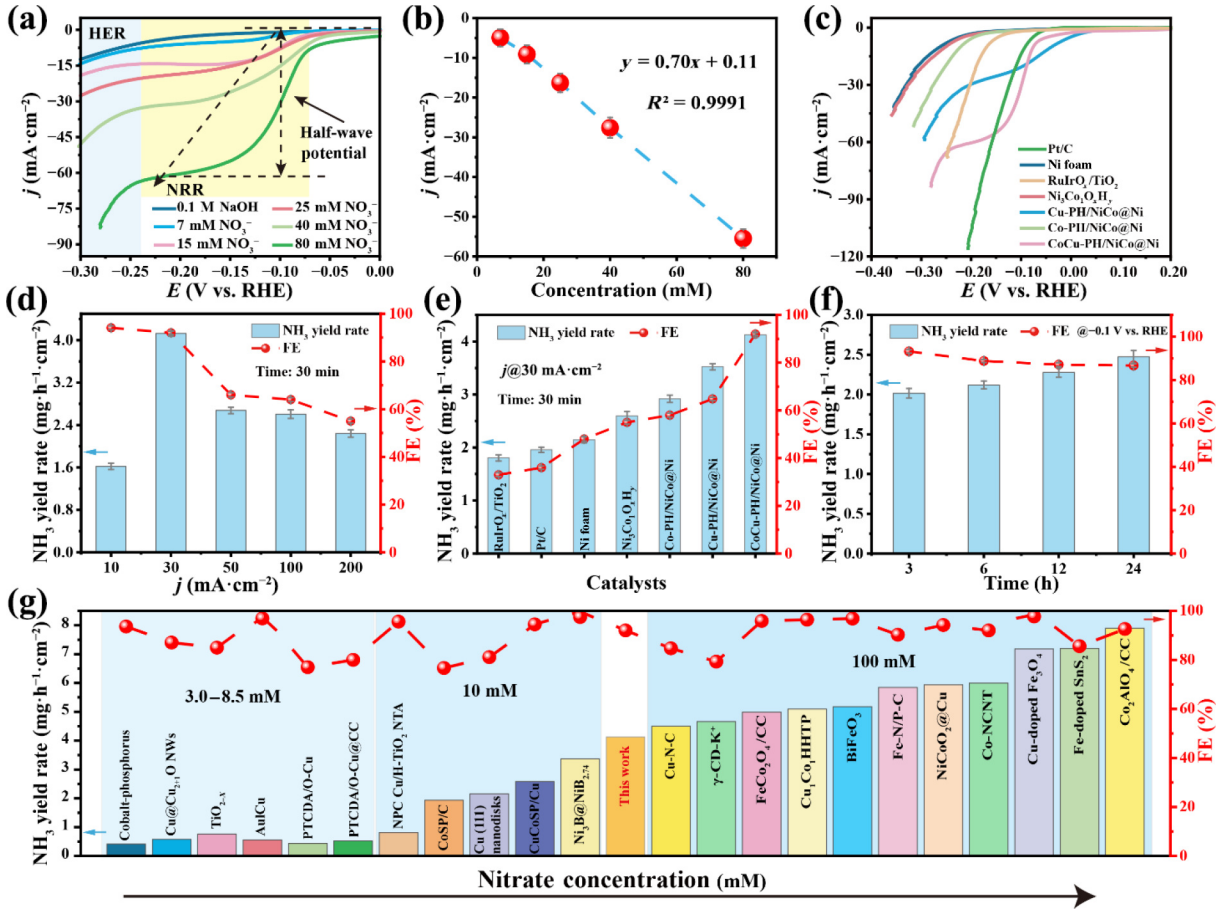

Figure 3 Electrocatalytic NO_3RR performance of CoCu-PH@NiCo/Ni. (a) The LSV curves of CoCu-PH@NiCo/Ni under different NO_3^- concentration. (b) Linear fitting of diffusion-limited current density and NO_3^- concentration. (c) The LSV curves of different materials in 0.1 M NaOH with 80 mM NO_3^-. (d) The R_{NH_3} and FE of CoCu-PH@NiCo/Ni at different current densities. (e) Comparison of R_{NH_3} and FE of different materials under fixed test conditions. (f) The variation of R_{NH_3} and FE at −0.1 V vs. RHE at different times. (g) Comparison of NO_3RR performance for various reported electrocatalysts. From left to right is sorted by nitrate concentration from lowest to highest.

PH/NiCo@Ni, we set the concentration of nitrate to be 40 mM, a concentration at which a relatively common contaminant is present in the industrial environment water and a level that can be achieved by proper concentration [47, 48]. At the same time, the detection method of related N-substances was established, as shown in Figs. S9–S11 in the ESM, corresponding to nitrate nitrogen (NO_3^--N), nitrite nitrogen (NO_2^--N) and ammonia nitrogen (NH_4^+-N) respectively. Firstly, we investigated the ammonia yield (R_{NH_3}) and FE at different current densities, as shown in Fig. 3(d). At a low current density of 10 mA·cm^{-2}, the FE is the highest up to 94.1%, but the R_{NH_3} is only 1.62 mg·h^{-1}·cm^{-2}. Notably, as the current density increases, the FE decreases continuously and when the current density reaches 50 mA·cm^{-2}, a value that can trigger the HER, the FE decreases to 66.3%. The highest R_{NH_3} is obtained at 30 mA·cm^{-2} with a value of 4.13 mg·h^{-1}·cm^{-2}. For a given catalyst, the FE is essentially limited by the NO_3^- concentration (diffusion limitation). At the same time, the Faraday efficiency and ammonia production data of nitrite NO_2^- and side reaction HER corresponding to CoCu-PH/NiCo@Ni at different current densities are shown in Fig. S12 in the ESM. As shown in Fig. S13 in the ESM, at a current density of 30 mA·cm^{-2}, the FE increases with concentration; in other words, high current density operation (implying high yields) can only be obtained by increasing mass transfer (either by increasing the concentration or by accelerating the diffusion of the mass transfer with additional energy consumption). Extremely high FE can be obtained by operating at low current density (< 5 mA·cm^{-2}), but this comes at the expense of yield rate. Remarkably, our prepared CoCu-PH/NiCo@Ni can achieve high R_{NH_3} at high current density while its FE can still reach 92.6%.

Subsequently, we compared the NO_3RR performance of the different materials at 30 mA·cm^{-2}, as shown in Fig. 3(e), both in terms of R_{NH_3} and FE, the prepared CoCu-PH/NiCo@Ni exhibited significant advantages, which validates the nature of its high NO_3RR activity. More interestingly, at a constant potential (−0.1 V vs. RHE), both R_{NH_3} and FE decrease with the increase of electrolysis time, as shown in Fig. 3(f), which can reach 2.47 mg·h^{-1}·cm^{-2} and 93.2% at the beginning. The recorded *j*–*t* curve is shown in Fig. S13 in the ESM, it can be found that the current density decreases with time and reaches a steady state (15 mA·cm^{-2}) after 4 h from the initial state of 25 mA·cm^{-2}.

It can be determined that this steady-state current is completely contributed by NO_3RR, as −0.1 V is not enough negative to trigger HER occurrence. In other words, at a low concentration of 40 mM, the three-dimensional porous electrode can provide a diffusion-limited current density of 15 mA·cm^{-2} under static conditions, unless an external force is provided, such as the use of a pump to accelerate the flow of liquid. The conversion of nitrate nitrogen at low concentrations is subject to diffusion control, Fig. 3(g)

illustrates the developed advanced catalysts for the NO_3RR (all the materials are listed in the Table S1 in the ESM), ranked in order of target concentration in the electrolyte from low to high, which follows an increase in R_{NH_3} with increasing concentration. Specifically, the prepared CoCu-PH/NiCo@Ni delivers an excellent performance with high R_{NH_3} of 4.13 mg·h^{-1}·cm^{-2} and FE of 92.6%, validated to be a competitive candidate for low concentration nitrates conversion.

2.4 *In situ* FT infrared (FTIR) and theoretical calculations

To understand the reaction intermediates and pathway of NO_3RR over the CoCu-PH/NiCo@Ni, the electrochemical *in situ* attenuated total reflectance FTIR (ATR-FTIR) spectra were performed. Figures 4(a) and 4(b) are the potential-dependent ATR-FTIR spectra with the applied potential from open circuit potential (OCP) to −0.4 V vs. RHE. The signal is almost undetectable at OCP, but new absorption bands appear when the negative potential (−0.05 V vs. RHE) that triggers NO_3RR is applied. These peaks' intensity increases with more negative potential. The two-dimensional contour image (Fig. 4(c)) depicts the dependence of the change in absorption bands on the applied potential. The detailed variations of peaks are shown in Fig. 4(d). The band at 1405 cm^{-1} can be assigned to the adsorption of NO_3^- [49–51] but noted that it is triggered at a potential of only 0.2 V, indicating that CoCu-PH/NiCo@Ni possesses excellent performance of NO_3^- adsorption. Besides, the adsorption band of H_2O^* (1650 cm^{-1}) also occurred at this potential. With the potential negatively moving to 0.1 V, an N–O antisymmetric stretching vibrational peak appears, which can be attributed to adsorbed NO_2^* [37, 52]. This indicates that NO_3^- deoxygenation to form NO_2^* requires a more negative potential to drive it. The bands at 1115, 2873 and 3150 cm^{-1} correspond to the stretching of N–H, N–H bending and NH_2 swing model of the formed NH_2^*, respectively [52–54]. These strong N–H peaks predict the formation of NH_3. The peak at 3000 cm^{-1} is attributed to the O–H bending of the adsorbed OH* [52, 55], which suggests that a dissociation of water molecules takes place. The protons provided by the dissociation of water molecules might be an important source for the deoxygenation of NO_3^{-*} and hydrogenation of N*.

To deeply understand the high activity of CoCu-PH/NiCo@Ni for the NO_3RR, the density functional theory (DFT) was employed to investigate reaction paths and intermediates state. According to our ATR-FTIR and previous reports [17], NO_3^- to NH_3 conversion on the electrode surface most likely includes: adsorption of NO_3^-, deoxygenation of the NO_3^{-*} and hydrogenation on the N* species (NO_3^-→NO_3^*→NO_2^*→NO*→N*→NH*→NH_2^*→NH_3^*→NH_3, the * represents the adsorption state and all the intermediate processes are the binding of the metal site to the N atom). The free energy diagram based on the Gibbs free energy change (Δ*G*) of the overall pathway for NO_3RR at 0 V vs. RHE at pH 13 is illustrated in Fig. 5(a). Previous studies revealed that the transition from NO_2^* to NO* requires a key transition state (TS) [56], called the formation of NO_2H^* (TS1). The formation of TS1 is related to adsorbed OH* in the neighbouring site, as shown in the insert crystal figure. The energy uphill of TS1 in CoCu-PH (0.12 eV) is lower than that of the monolithic site of Cu-PH (0.44 eV), suggesting that the former can efficiently provide the OH*. The underlying discrepancy may be related to the fact that Co sites have a better ability to facilitate the decomposition of adsorbed H_2O, or in other words, appropriate HER activity may reduce the energy barrier of the formation of NO_2H^*. The potential difference may be related to the better ability of Co sites to promote the decomposition of adsorbed H_2O, or in other words, appropriate HER activity may reduce the energy barrier for the formation of NO_2H^*. The process of Co sites promoting hydrolysis and dissociation to form OH* is usually closely related to the charge transfer, proton transfer, adsorption and dissociation of reactant molecules on the electrode surface. After the water molecule H_2O accepts electrons on the surface of the catalyst, it can be dissociated into hydroxide ion OH^- through the Volmer–Heyrovsky reaction path and adsorbs the hydrogen atom H* [57, 58]. Coupled with the unique electronic structure and catalytic activity of the Co site, this dissociation process can be

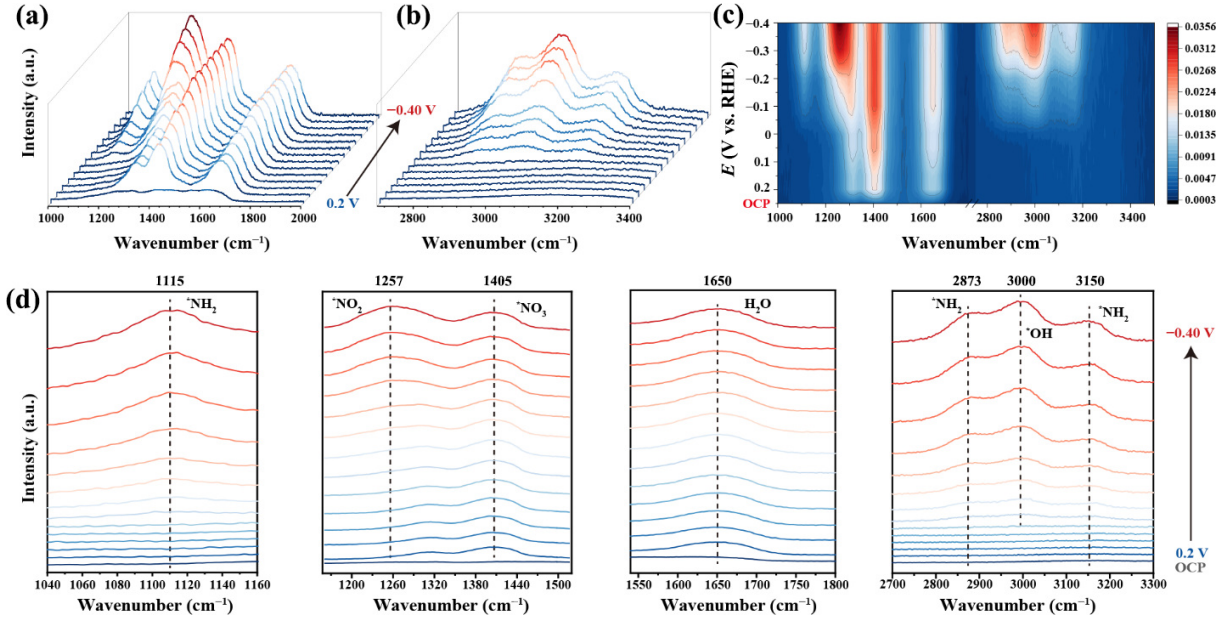

Figure 4 Potential-dependent *in situ* ATR-FTIR spectra. (a) and (b) The electrochemical *in situ* ATR-FTIR spectra for CoCu-PH/NiCo@Ni electrode conducted in 0.1 M NaOH + 40 mM NO_3^-. electrolyte. (c) The corresponding contour image of CoCu-PH/NiCo@Ni at different applied potentials. (d) Local plots of *in situ* ATR-FTIR spectra.

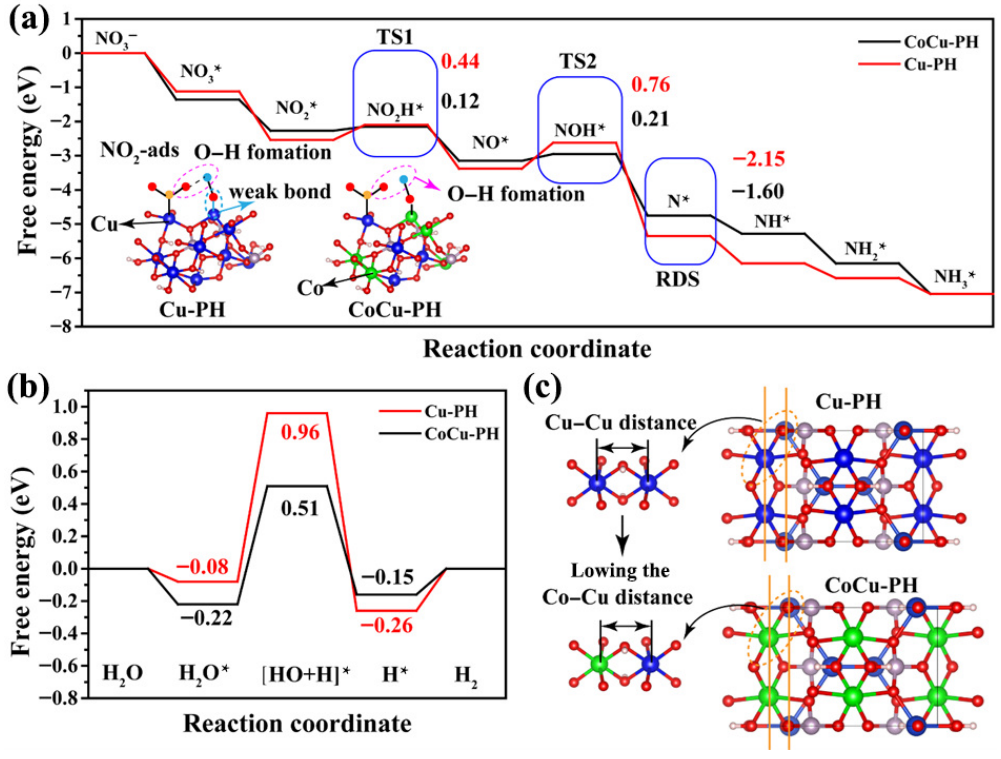

Figure 5 Theoretical analyses of the catalytic mechanism of NO_3RR over the CoCu-PH surface. (a) Free energy diagram of each intermediate state on the Cu/Co metal sites. Two key intermediate transition states (TS1 and TS2) are also included. The insert adsorption crystal structure corresponds to the TS1. There is a similar structure for TS2. (b) Free energy diagram for HER on the surface of CoCu-PH. (c) Comparison of the crystal structures of Cu-PH and CoCu-PH. Based on the EXAFS results, it is hypothesized that the metal–metal distance of the binary material may be reduced.

accelerated, so that more water molecules are activated into O–H bonds in the H_2O molecule, making it easier to break to form OH* [59].

To validate this, the Volmer–Heyrovsky reaction path is used to calculate the free energy of HER in alkaline conditions, as shown in Fig. 5(b). It can be found that the Volmer step, which adsorbed H_2O* dissociated into adsorbed OH* and H* intermediate is the rate-determined step (RDS) [60] and an energy barrier (ΔG_{H-OH}) of up to 1.04 eV needs to be overcome om the Cu-PH surface, while ΔG_{H-OH} is reduced to 0.73 eV on the binary CoCu-PH surface. These results demonstrate that the binary of Co-Cu can substantially accelerate the kinetics of the water dissociation and provide the OH* that is urgently needed for the TS1 process. Back to the NO_3RR, another key step is the NO*→N*, which undergoes a TS of NOH* (TS2), which also requires the neighbouring site to be able to provide an adsorbed state of OH*. This step is similar to the TS1 process but gives rise to a higher energy barrier and is regarded as the RDS for alkaline NO_3RR [61]. An uphill to 0.76 eV is predicted in the energy profile of Cu-PH, which is much higher than that of Co-Cu (0.21 eV), evidencing that the binary catalytic site with strong water dissociation ability can better promote the activity of NO_3RR. Although CoCu-PH has a strong H_2O* dissociated capacity, this does not imply that HER occurs preferentially on its surface over NO_3RR, because the energy barrier for the HER (0.73 eV) is higher than that of the RDS of the NO_3RR. Moreover, the Gibbs energy for NO_3^- absorption (−1.36 eV) is much lower than that for H_2O absorption (−0.22 eV), suggesting that NO_3^- is much easier to adsorb on the CoCu-PH surface than H_2O. A somewhat enhanced HER activity of the catalyst is beneficial for enhancing the NO_3RR, which is consistent with the previously revealed [62]. In turn, it is to be expected that an increase in Co content will inevitably bring about an increase in HER activity, which is then detrimental to the conversion of NO_3^-. It is evidenced by our designed catalysts with high Co content of Co_4Cu_1-PH and Co_3Cu_1-PH (Fig. S14 in the ESM) and therefore the Co/Cu ratio must be adjusted to maximize the advantages of the dissociation of water molecules.

As revealed by the DFT, both the deoxygenation and the subsequent hydrogenation processes of the N-species involve the delivery of proton. Functionalization of dual-site of the catalysts is crucial for enhancing NO_3RR activity, i.e., one of the sites can play the role of a proton provider. Therefore, the catalyst may need to perform adsorption and dissociation on both molecules (here, NO_3^- and H_2O), with mutual bonding occurring in the appropriate intermediate states. For the TS2, an RDS for NO_3RR, the bonding formation may be *–NOH–H–OH–*. The formation of this intermediate state may be bonded with hydrogen bonding. As a result, the distance between the dual sites becomes crucial for the effective formation of hydrogen bonds. As mentioned by k^2-FTEXAFS, a compression effect is present over the binary CoCu-PH, which means the distance between Co–Cu is lower than the Cu–Cu distance on the Cu-PH. This effect of crystal structure shrinkage is shown in Fig. 5(c). The lower Co–Cu distance can effectively promote the formation of hydrogen bonds, which are responsible for the reduction of the energy barrier for TS.

2.5 Long-term stability evaluation

The long-term stability of prepared CoCu-PH/NiCo@Ni was evaluated by the chronoamperometry in an H-type cell at −0.1 V vs. RHE. As shown in Fig. 6(a), the current density exhibits a similar tendency as observed in Fig. S13 in the ESM, which will reach a

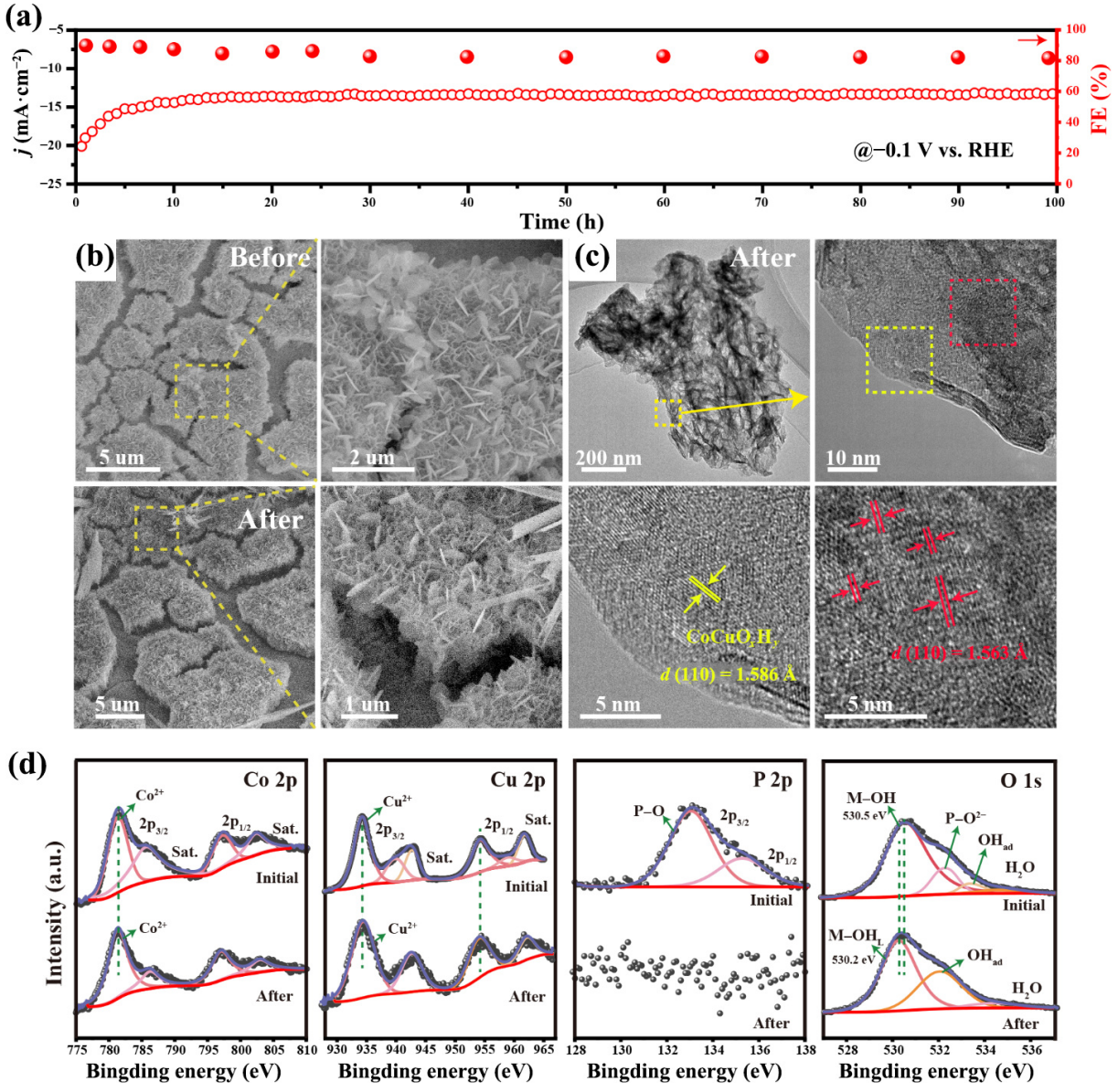

Figure 6 Stability evaluation of CoCu-PH@NiCo/Ni. (a) The long-term chronoamperometry test of CoCu-PH@NiCo/Ni at −0.1 V vs. RHE in 0.1 M NaOH with 40 mM NO_3^-. (b) The SEM images of the initial and after stability test. (c) The TEM images of the after-stability test and the HRTEM images corresponding to the selected region. (d) The XPS spectra of Co 2p, Cu 2p, P 2p and O 1s.

steady state after a few hours. During the steady state operation, there is no appreciable decrease in current density, indicating that the CoCu-PH/NiCo@Ni possesses good stability. In addition, it still maintains a high FE of 83% over 100 h of continuous operation. After the stability test, there is little difference in activity before and after as revealed by post-linear sweep voltammetry (LSV) (Fig. S15 in the ESM), which confirms that the CoCu-PH/NiCo@Ni has good stability. To verify that the catalytic electrode of CoCu-PH/NiCo@Ni has a stable ammonia production capacity, the long-term cycling test with 20 cycles (continuous electrolysis for 6 h per cycle) was conducted. As shown in Fig. S16 in the ESM, the R_{NH_3} fluctuated around 4.1 mg·h^{-1}·cm^{-2}, while FE was higher than 82% in multiple cycle tests, further indicating excellent stability of CoCu-PH/NiCo@Ni.

The performed XRD patterns also verified that the CoCu-PH/NiCo@Ni maintains structure stability as the diffraction peaks are essentially the same as the initial (Fig. S17 in the ESM). Moreover, the post-scanning electron microscopy (SEM) and HRTEM are conducted to observe whether the morphology of the embedded structure of the CoCu-PH/NiCo@Ni changes under long-term operation. By comparison of the SEM images (Fig. 6(b)), it can be seen that the surface morphological features of CoCu-PH embedded in the interlayer $Ni_3Co_1O_xH_y$ are the same as those of the initial one. Figure 6(c) shows the HRTEM images with different magnifications, the overall embedded structure remains well after long-term operation, indicating that the reduction of nitrate did not destroy its morphological structure. Besides, we note that the facets lattice exposed by the surface beyond the hydroxy phosphates of binary CoCu-PH, instead is more in line with the (110) facets of the mixed oxy/hydroxides of Co and Cu, since the distance space exposed of the surface is 1.586 Å. As observed in the HRTEM, the initial catalytic component of CoCu-PH may have undergone a phase transition, called surface reconstruction, during the long-term operation.

To furtherly verify the surface reconstruction of CoCu-PH/NiCo@Ni, the surface X-ray photoelectron spectroscopy (XPS) is performed and the full spectra of CoCu-PH/NiCo@Ni and C-calibration are shown in Fig. S18 in the ESM. Figure 6(d) shows the deconvoluted spectra of Co 2p, in which the peak of Co $2p_{3/2}$ with the binding energy of 781.14 eV can be assigned to the Co^{2+} state [63]. The position of the main peaks of Co $2p_{3/2}$ and Co $2p_{1/2}$ after stability is consistent with the initial one, indicating that the valence state of Co does not change. However, we note that the spectrum shape has changed result of the weakening of the satellite peak intensity. The strong intensity of the satellite peaks is related to the high spin of Co^{2+}, which is common in Co-Pi materials [64] and thus the weakening of their strength is most likely associated with the loss of phosphate coordination. For the comparison of Cu 2p spectra, there are no significant shifts in the binding energy of main peaks, suggesting that the valence state of Cu may not have been affected by the reduction conditions. It is worth noting that the P 2p from the phosphate ligand is lost after a long operation of 100 h. The loss of P-specie may imply that CoCu-PH underwent a surface reconstruction process, which is evidenced by O 1s XPS. The surface oxygen species after long-term operation are essentially dominated by lattice hydroxyls (M–OH, M: metal) and the P–O species located at 531.4 eV corresponding to phosphate ligand are essentially lost, which suggests that the loss of phosphate during surface reconstruction may be accompanied by the formation of hydroxides [65–68]. These observations are also verified by Raman spectra, as shown in Fig. S19 in the ESM, the ligand of phosphate is disappearance, while the CoCu–O/OH coordination is preserved well. Therefore, it is reasonably believed that the phosphate is derived from MO_x/M(OH)$_x$ or MOOH on the surface. Although the absence of HER, surface reconstruction of the phosphate still happens, suggesting that there may be a process involved in the adsorption and disassociation of water molecules. This validates our speculation that the catalytic site is needed to activate the water molecule to provide the necessary protons for the deoxygenation and hydrogenation for the conversion of nitrate to ammonia.

3 Conclusion

In short, a novel 3D CoCu-PH/NiCo@Ni electrode with embedded binary CoCu-PH is rationally designed for nitrate electrochemical reduction. It delivers a high R_{NH_3} of 4.13 mg·h^{-1}·cm^{-2} with a high FE of 92.6% at a moderate current density of 30 mA·cm^{-2} under a low nitrate concentration of 40 mM. The impressive NO_3RR performance over the CoCu-PH/NiCo@Ni can be maintained for 100 h at a potential of −0.1 V vs. RHE. With the aid of XAFS, we demonstrate the host structure includes valence states and coordination symmetry are modified accompanied by Cu doping. The performed DFT indicated the binary CoCu-PH can effectively reduce the energy barrier of the RDS in the NO_3RR process and the ability of regulated adsorption strength can be attributed to the water dissociation at the Co site. We emphasize that the adsorbed OH* intermediates at the Co site can provide abundant protons for the formation of NO_2H* and subsequent hydrogenation at N*. Moreover, benefiting from the incorporation of heterogeneous elements, the atomic spacing is shortened, thus providing shorter hydrogen bonds for the formation of key intermediates. Overall, this work provides an alternative strategy based on multi-architecture and binary components to design highly efficient NO_3RR catalysts for low-concentration nitrates conversion to ammonia.

4 Experimental section/methods

4.1 Synthesis of catalysts

All chemical reagents are analytically pure without specific instructions. The aqueous solution used in the synthesis process is ultra-pure water. A piece of commercial Ni foam was cut into 3.5 × 3.5 cm and was immersed in 3 M HCl solution for 20 min to remove the oxides on the surface and then washed ultrasonically with ethanol absolute and deionized water separately. The intermediate of $Ni_3Co_1O_xH_y$ was electrodeposited on the pre-treated Ni foam. Briefly, in a preset solution containing 0.3 M cobalt nitrate Co $(NO_3)_2$ and 0.1 M nickel nitrate Ni $(NO_3)_2$, $Ni_3Co_1O_xH_y$@Ni was prepared by applying 70 mA constant current electrodeposition for 300 s using Ni foam as the cathode.

A typical hydrothermal method was used to prepare the CoCu-PH/NiCo@Ni. The metal ion precursor is the corresponding nitrate and its Co:Cu molar ratio is set to 2:1 and mixed in the 100 mL Teflon-lined pressure vessel. After that, 500 mg PVP was added into the solution and ultrasonic dispersion for 30 min to completely dissolve. Then, 1 mmol $(NH_4)_2HPO_4$ acts as a phosphate precursor was slowly dripped into the mixture solution and the as-synthesized $Ni_3Co_1O_xH_y$@Ni was placed diagonally in the hydrothermal reactor. Noted that, the order of adding PVP and $(NH_4)_2HPO_4$ cannot be reversed. After sealing and heating at 180 °C for 12 h, the as-synthesized CoCu-PH/NiCo@Ni was taken out, washed ultrasonically and dried overnight. The preparation method of Co-PH/NiCo@Ni and Cu-PH/NiCo@Ni is consistent with the above. For preparation of $RuIrO_x$/Ti, the mix precursors with Ru:Ir = 3:1 were uniformly coated over Ti, then dried and placed in a furnace at 400 °C for 10 min and the process was repeated four times until the coating amount reached 0.2 mg·cm^{-2}.

4.2 Electrochemical characterizations:

All electrochemical tests were carried out with a three-electrode system using a CHI760E (Shanghai Chenhua, China) and programmable direct current (DC) power supply (Henghui HSP-3030) in a 0.1 M NaOH + 40 mM NO_3^-. Here, the prepared sample is used as a working electrode; a platinum plate electrode with an area of 1 cm^2 is used as a counter electrode. The standard Hg/HgO electrode was used as the reference electrode. The potential (E) versus Hg/HgO scale was converted into a RHE standard by Nernst equation calibration

$$E(\text{vs. RHE}) = E(\text{vs. Hg/HgO}) + 0.098\ \text{V} + 0.0592 \times \text{pH}$$

The reducibility of nitrate with *ir*-corrected (*i*: current and *r*: solution resistance) was investigated by LSV with a low scan rate of 5 mV·s^{-1} to understand the true properties of the material. The redox peak potentials of different electrode materials were tested by cyclic voltammetry (CV) to understand the reaction mechanism of the materials. EIS was used to test at −0.1 V vs. RHE, with a potential amplitude of 10 mV and a frequency range of 1–10^6 Hz that fit the Nyquist plot, the resistance and charge transfer resistance are obtained.

4.3 Determination of the concentration of N-containing species

The ultraviolet–visible (UV–Vis) absorbance spectra were measured on a PERSEE TU-1950 UV–Vis spectrophotometer. Ammonia-N (NH_4^+-N) was measured by Nessler's reagent

spectrophotometry [69]. Due to the slightly higher concentration of the cathode solution, it was diluted before the test. The diluted water sample of 2.5 mL was added with 2 mL of 2% potassium sodium tartrate ($NaKC_4H_4O_6$). After mixing, 0.5 mL of Nessler's reagent was added for color reaction. After 20 min, the absorbance was measured at 420 nm wavelength under an ultraviolet–visible spectrophotometer. The concentration of NH_4^+-N was determined by substituting it into the standard curve of ammonia nitrogen and then the concentration of NH_3 was calculated.

Nitrite-N (NO_2^--N) was measured using ultraviolet–visible absorption spectrum [70]. 2 mL diluted water sample was mixed with 1 mL R_1 (p-aminobenzene sulfonamide mixed solution) and then 1 mL R_2 N-(1-naphthyl) ethylenediamine dihydrochloride, solution) was added. The absorbance was measured at 540 nm wavelength within 30 min after shaking and mixing and the concentration of nitrite nitrogen was determined according to the standard curve.

Nitrate-N (NO_3^--N) was determined by ultraviolet–visible spectrophotometry [15, 70]. Take 0.1 mL 1 M HCl and 0.01 mL 0.8 wt.% sulfamic acid solution were added to the test solution. The wavelength is measured at 220 and 275 nm and the absorbance (A) of NO_3^--N is calculated according to the following formula $A = A_{220\,nm} - A_{275\,nm}$ and the actual concentration of nitrate is calculated in the standard curve.

4.4 The yield and Faradaic efficiency

For the nitrate (NO_3^-) reduction reactions, the FE and NH_3 yield rate is calculated as follows

$$FE = \frac{8 \times F \times [NH_3] \times V}{M_{NH_3} \times Q} \times 100\%$$

$$R_{NH_3} = \frac{[NH_3] \times V}{M_{NH_3} \times t \times A}$$

where F is the Faradic constant (96,485 C·mol^{-1}), $[NH_3]$ is the measured NH_3 concentration, V is the volume of electrolyte in the cathode compartment, M_{NH_3} is the molar mass of NH_3, Q is the total quantity of applied electricity, t is the electrolysis time and A is the working area of the catalyst.

4.5 Material characterizations:

The crystal structure of the catalysts was investigated using XRD measurement equipped with a D/max2550 V apparatus and a Cu-Kα radiation source (λ = 1.5406 Å) and the data were recorded from 10° to 80° at the step size of 0.02°. The morphology and composition of the samples were characterized by field emission SEM (FE-SEM, Verios G4UC) combined with energy-dispersive X-ray spectroscopy (EDS). The micromorphology was studied by TEM (Talos F200X G2). The surface composition and element valence state of the samples were determined by ESCALAB 250Xi XPS with a high-resolution XPS spectrum obtained at an energy step of 0.05 eV. All deconvolutional high-resolution XPS spectra were calibrated by C-1 s at 284.8 eV. The XAS data of the samples were recorded at room temperature in fluorescence mode using ion chambers in the Shanghai Synchrotron Radiation Facility (SSFR, beamline BL14W1, Shanghai) and National Synchrotron Radiation Laboratory (NSRL, beamline BL11U, Hefei), China. The station was operated with a Si (111) double crystal monochromator. During measurements, the synchrotron was operated at the energy of 3.5 GeV and the current varied between 150 and 210 mA.

4.6 *In situ* external reflection FTIR analysis

Electrochemical FTIR spectroscopy measurements and IR reflection-absorption spectroscopy (IRRAS) measurements were performed by a Nicolet IS50 spectrometer with an electrochemical workstation and an H-type electrolytic cell. The prepared CoCu-PH/NiCo@Ni electrode was used as the working electrode, Hg/HgO as the reference electrode and Pt as the counter electrode. The nitrate reduction test was performed in a mixed solution of 0.1 M NaOH and 40 mM NO_3^- and the spectra were collected at 50 mV per point at open circuit potential and 0.2 to −0.4 V vs. RHE potential. The spectral resolution of all measurements is 4 cm^{-1}. The obtained spectrum is used as the relative change of reflectivity (ΔR)

$$\Delta R/R_0 = (R - R_0)/R_0$$

where R is the reflectivity at the sample potential and R_0 is the reflectivity at the reference potential.

4.7 DFT calculation methods

All first-principal calculations were performed using the DFT methodology implemented in the Vienna *ab-initio* simulation package (VASP). The spin-polarized projector augmented wave (PAW) method [71, 72] and the Perdew–Burke–Ernzerhof (PBE) [73, 74] electron exchange-correlation functional of the generalized gradient approximation (GGA) were used in these calculations. The energy cutoff for the wave function expanding in the plane-wave basis was set to 400 eV. The energetic convergence threshold for the self-consistent field was 1 × 10^{-5} eV·atom^{-1}. The structure optimization force threshold was set to 0.02 eV·Å^{-1}. The $Co_2(OH)PO_4$ with a crystal parameter of 8.042 × 8.369 × 5.94 (90.0 × 90.0 × 90.0) was used to host structure for constructing the CoCu-PH, in which the Co sites are replaced by Cu in a mole ratio of Co:Cu = 2:1. The Brillouin-zone integrations were calculated using Monkaorst–Pack grids with (2 × 2 × 1) mesh. A vacuum slab of 15 Å was used in the model. The Gibbs free energy profile of NO_3RR is modeled at the (220) crystal surface of CoCu-PH. This surface termination was chosen as they are observed from the HRTEM images and represent low-energy surfaces. The free energies of adsorption of the NO_3RR and HER are calculated from $\Delta G = \Delta E + \Delta ZPE - T\Delta S$, where ΔE is the total energy, ΔZPE is the zero-point energy, T is the temperature in Kelvin and ΔS is the entropy. Adsorption-freebies are calculated by using NO_3^- and H_2O as references as well as considering zero-point energy and entropy corrections at T = 298.15 K.

Electronic Supplementary Material: Supplementary material is available in the online version of this article at https://doi.org/10.26599/NR.2025.94907048.

Data availability

All data needed to support the conclusions in the paper are presented in the manuscript and the Electronic Supplementary Material. Additional data related to this paper may be requested from the corresponding author upon request.

Acknowledgements

This work was financially supported by Hainan Province Science and Technology Special Fund (No. ZDYF2023GXJS165), National Natural Science Foundation of China (No. 22102042) and Hainan

Province Key Scientific Research Project (No. ZDYF2021GXJS026). The authors would like to thank Shanghai Synchrotron Radiation Facility (SSFR, beamline BL14W1, Shanghai) and National Synchrotron Radiation Laboratory (NSRL, beamline BL11U, Hefei) for providing the beam times. We also would like to thank the Analytical and Testing Center of Hainan University and the State Key Laboratory of Marine Resource Utilization in the South China Sea for providing characterization instruments.

Declaration of competing interest

All the contributing authors report no conflict of interests in this work.

Author contribution statement

C. Z.: Writing – original draft, methodology, investigation, data curation, conceptualization. Y. F. Y.: Formal analysis, conceptualization. Y. K. J.: Investigation. Z. Z.: Investigation. X. S. Y.: supervision, software. W. S.: Writing – review & editing, validation, supervision, software, resources. F. Y.: Validation, supervision, methodology, conceptualization. All the authors have approved the final manuscript.

Use of AI statement

None.

References

[1] Wang, Y. T.; Yu, Y. F.; Jia, R. R.; Zhang, C.; Zhang, B. Electrochemical synthesis of nitric acid from air and ammonia through waste utilization. *Natl. Sci. Rev.* **2019**, *6*, 730–738.

[2] Zeng, Y. C.; Priest, C.; Wang, G. F.; Wu, G. Restoring the nitrogen cycle by electrochemical reduction of nitrate: Progress and prospects. *Small Methods* **2020**, *4*, 2000672.

[3] Truong, N. H.; Kim, J. S.; Lim, J.; Shin, H. Electrochemical reduction of nitrate to Ammonia: Recent progress and future directions. *Chem. Eng. J.* **2024**, *495*, 153108.

[4] van Langevelde, P. H.; Katsounaros, I.; Koper, M. T. M. Electrocatalytic nitrate reduction for sustainable ammonia production. *Joule* **2021**, *5*, 290–294.

[5] Xiong, Y. C.; Wang, Y. H.; Zhou, J. W.; Liu, F.; Hao, F. K.; Fan, Z. X. Electrochemical nitrate reduction: Ammonia synthesis and the beyond. *Adv. Mater.* **2024**, *36*, 2304021.

[6] Lu, X. M.; Song, H. Q.; Cai, J. M.; Lu, S. Y. Recent development of electrochemical nitrate reduction to ammonia: A mini review. *Electrochem. Commun.* **2021**, *129*, 107094.

[7] Ren, S. J.; Gao, R. T.; Nguyen, N. T.; Wang, L. Enhanced charge carrier dynamics on Sb_2Se_3 photocathodes for efficient photoelectrochemical nitrate reduction to ammonia. *Angew. Chem., Int. Ed.* **2024**, *63*, e202317414.

[8] Wang, M.; Khan, M. A.; Mohsin, I.; Wicks, J.; Ip, A. H.; Sumon, K. Z.; Dinh, C. T.; Sargent, E. H.; Gates, I. D.; Kibria, M. G. Can sustainable ammonia synthesis pathways compete with fossil-fuel based Haber–Bosch processes. *Energy Environ. Sci.* **2021**, *14*, 2535–2548.

[9] Duca, M.; Koper, M. T. M. Powering denitrification: The perspectives of electrocatalytic nitrate reduction. *Energy Environ. Sci.* **2012**, *5*, 9726–9742.

[10] Wang, Y. T.; Wang, C. H.; Li, M. Y.; Yu, Y. F.; Zhang, B. Nitrate electroreduction: Mechanism insight, *in situ* characterization, performance evaluation, and challenges. *Chem. Soc. Rev.* **2021**, *50*, 6720–6733.

[11] Sun, W. J.; Ji, H. Q.; Li, L. X.; Zhang, H. Y.; Wang, Z. K.; He, J. H.; Lu, J. M. Built-in electric field triggered interfacial accumulation effect for efficient nitrate removal at ultra-low concentration and electroreduction to ammonia. *Angew. Chem., Int. Ed.* **2021**, *60*, 22933–22939.

[12] Song, Q. N.; Li, M.; Hou, X. S.; Li, J. C.; Dong, Z. J.; Zhang, S.; Yang, L.; Liu, X. Anchored Fe atoms for N=O bond activation to boost electrocatalytic nitrate reduction at low concentrations. *Appl. Catal. B* **2022**, *317*, 121721.

[13] Wu, Y. D.; Lu, K. K.; Xu, L. H. Progress and prospects of electrochemical reduction of nitrate to restore the nitrogen cycle. *J. Mater. Chem. A* **2023**, *11*, 17392–17417.

[14] Xu, H.; Ma, Y. Y.; Chen, J.; Zhang, W. X.; Yang, J. P. Electrocatalytic reduction of nitrate—A step towards a sustainable nitrogen cycle. *Chem. Soc. Rev.* **2022**, *51*, 2710–2758.

[15] Wang, Y. T.; Zhou, W.; Jia, R. R.; Yu, Y. F.; Zhang, B. Unveiling the activity origin of a copper-based electrocatalyst for selective nitrate reduction to ammonia. *Angew. Chem., Int. Ed.* **2020**, *59*, 5350–5354.

[16] Zhao, Y. X.; Liang, S. Z.; Zhao, Y. J.; Zhang, H. J.; Zheng, X.; Li, Z. Q.; Chen, L. S.; Tang, J. Hollow mesoporous carbon supported Co-modified Cu/Cu_2O electrocatalyst for nitrate reduction reaction. *J. Colloid Interface Sci.* **2024**, *655*, 208–216.

[17] Chen, F. Y.; Wu, Z. Y.; Gupta, S.; Rivera, D. J.; Lambeets, S. V.; Pecaut, S.; Kim, J. Y. T.; Zhu, P.; Finfrock, Y. Z.; Meira, D. M. et al. Efficient conversion of low-concentration nitrate sources into ammonia on a Ru-dispersed Cu nanowire electrocatalyst. *Nat. Nanotechnol.* **2022**, *17*, 759–767.

[18] Hao, R.; Tian, L.; Wang, C.; Wang, L.; Liu, Y. P.; Wang, G. C.; Li, W.; Ozin, G. A. Pollution to solution: A universal electrocatalyst for reduction of all NO_x-based species to NH_3. *Chem Catal.* **2022**, *2*, 622–638.

[19] Zhang, X.; Wang, C. H.; Guo, Y. M.; Zhang, B.; Wang, Y. T.; Yu, Y. F. Cu clusters/TiO_{2-x} with abundant oxygen vacancies for enhanced electrocatalytic nitrate reduction to ammonia. *J. Mater. Chem. A* **2022**, *10*, 6448–6453.

[20] Zhao, X.; Hu, G. Z.; Tan, F.; Zhang, S. S.; Wang, X. Z.; Hu, X.; Kuklin, A. V.; Baryshnikov, G. V.; Ågren, H.; Zhou, X. H.; Zhang, H. B. Copper confined in vesicle-like BCN cavities promotes electrochemical reduction of nitrate to ammonia in water. *J. Mater. Chem. A* **2021**, *9*, 23675–23686.

[21] Liu, H. M.; Lang, X. Y.; Zhu, C.; Timoshenko, J.; Rüscher, M.; Bai, L. C.; Guijarro, N.; Yin, H. B.; Peng, Y.; Li, J. H. et al. Efficient electrochemical nitrate reduction to ammonia with copper-supported rhodium cluster and single-atom catalysts. *Angew. Chem., Int. Ed.* **2022**, *61*, e202202556.

[22] Wang, W. Y.; Chen, J.; Tse, E. C. M. Synergy between Cu and Co in a layered double hydroxide enables close to 100% nitrate-to-ammonia selectivity. *J. Am. Chem. Soc.* **2023**, *145*, 26678–26687.

[23] Wang, Y. H.; Xu, A. N.; Wang, Z. Y.; Huang, L. S.; Li, J.; Li, F. W.; Wicks, J.; Luo, M. C.; Nam, D. H.; Tan, C. S. et al. Enhanced nitrate-to-ammonia activity on copper-nickel alloys via tuning of intermediate adsorption. *J. Am. Chem. Soc.* **2020**, *142*, 5702–5708.

[24] Liu, P.; Yan, J. Y.; Huang, H.; Song, W. B. Cu/Co bimetallic conductive MOFs: Electronic modulation for enhanced nitrate reduction to ammonia. *Chem. Eng. J.* **2023**, *466*, 143134.

[25] Wang, J.; Feng, T.; Chen, J. X.; Ramalingam, V.; Li, Z. X.; Kabtamu, D. M.; He, J. H.; Fang, X. S. Electrocatalytic nitrate/nitrite reduction to ammonia synthesis using metal nanocatalysts and bio-inspired metalloenzymes. *Nano Energy* **2021**, *86*, 106088.

[26] Liu, D.; Qiao, L. L.; Peng, S. Y.; Bai, H. Y.; Liu, C. F.; Ip, W. F.; Lo, K. H.; Liu, H. C.; Ng, K. W.; Wang, S. P. et al. Recent advances in

electrocatalysts for efficient nitrate reduction to ammonia. *Adv. Funct. Mater.* **2023**, *33*, 2303480.

[27] Jung, W.; Hwang, Y. J. Material strategies in the electrochemical nitrate reduction reaction to ammonia production. *Mater. Chem. Front.* **2021**, *5*, 6803–6823.

[28] Zhao, H.; Yuan, Z. Y. Insights into transition metal phosphate materials for efficient electrocatalysis. *ChemCatChem* **2020**, *12*, 3797–3810.

[29] Guo, R. H.; Lai, X. X.; Huang, J. W.; Du, X. C.; Yan, Y. C.; Sun, Y. H.; Zou, G. F.; Xiong, J. Phosphate-based electrocatalysts for water splitting: Recent progress. *ChemElectroChem* **2018**, *5*, 3822–3834.

[30] Zhao, H.; Yuan, Z. Y. Design strategies of transition-metal phosphate and phosphonate electrocatalysts for energy-related reactions. *ChemSusChem* **2021**, *14*, 130–149.

[31] Kanan, M. W.; Nocera, D. G. *In situ* formation of an oxygen-evolving catalyst in neutral water containing phosphate and Co^{2+}. *Science* **2008**, *321*, 1072–1075.

[32] Wang, J. H.; Cui, W.; Liu, Q.; Xing, Z. C.; Asiri, A. M.; Sun, X. P. Recent progress in cobalt-based heterogeneous catalysts for electrochemical water splitting. *Adv. Mater.* **2016**, *28*, 215–230.

[33] Gerken, J. B.; McAlpin, J. G.; Chen, J. Y. C.; Rigsby, M. L.; Casey, W. H.; Britt, R. D.; Stahl, S. S. Electrochemical water oxidation with cobalt-based electrocatalysts from pH 0–14: The thermodynamic basis for catalyst structure, stability, and activity. *J. Am. Chem. Soc.* **2011**, *133*, 14431–14442.

[34] Kim, H.; Park, J.; Park, I.; Jin, K.; Jerng, S. E.; Kim, S. H.; Nam, K. T.; Kang, K. Coordination tuning of cobalt phosphates towards efficient water oxidation catalyst. *Nat. Commun.* **2015**, *6*, 8253.

[35] Liu, Z. C.; Yuan, X. H.; Zhang, S. S.; Wang, J.; Huang, Q. H.; Yu, N. F.; Zhu, Y. S.; Fu, L. J.; Wang, F. X.; Chen, Y. H. et al. Three-dimensional ordered porous electrode materials for electrochemical energy storage. *NPG Asia Mater.* **2019**, *11*, 12.

[36] Huang, Y. M.; He, C. H.; Cheng, C. Q.; Han, S. H.; He, M.; Wang, Y. T.; Meng, N. N.; Zhang, B.; Lu, Q. P.; Yu, Y. F. Pulsed electroreduction of low-concentration nitrate to ammonia. *Nat. Commun.* **2023**, *14*, 7368.

[37] Huang, Y. M.; Long, J.; Wang, Y. T.; Meng, N. N.; Yu, Y. F.; Lu, S. Y.; Xiao, J. P.; Zhang, B. Engineering nitrogen vacancy in polymeric carbon nitride for nitrate electroreduction to ammonia. *ACS Appl. Mater. Interfaces* **2021**, *13*, 54967–54973.

[38] Polcaro, A. M.; Mascia, M.; Palmas, S.; Vacca, A. Electrochemical oxidation of p-hydroxybenzoic and protocathecuic acids at a dimensional stable anode (DSA) in the presence of NaCl. *Ann. Chim.* **2002**, *92*, 1015–1023.

[39] Lu, Y. X.; Zhou, L.; Wang, S. Y.; Zou, Y. Q. Defect engineering of electrocatalysts for organic synthesis. *Nano Res.* **2023**, *16*, 1890–1912.

[40] Guo, W.; Dun, C. C.; Yu, C.; Song, X. D.; Yang, F. P.; Kuang, W. Z.; Xie, Y. Y.; Li, S. F.; Wang, Z.; Yu, J. H. et al. Mismatching integration-enabled strains and defects engineering in LDH microstructure for high-rate and long-life charge storage. *Nat. Commun.* **2022**, *13*, 1409.

[41] Li, J.; Li, Y.; Routh, P. K.; Makagon, E.; Lubomirsky, I.; Frenkel, A. I. Comparative analysis of XANES and EXAFS for local structural characterization of disordered metal oxides. *J. Synchrotron Rad.* **2021**, *28*, 1511–1517.

[42] Fabbri, E.; Abbott, D. F.; Nachtegaal, M.; Schmidt, T. J. *Operando* X-ray absorption spectroscopy: A powerful tool toward water splitting catalyst development. *Curr. Opin. Electrochem.* **2017**, *5*, 20–26.

[43] Zhu, K. Y.; Zhu, X. F.; Yang, W. S. Application of *in situ* techniques for the characterization of NiFe-based oxygen evolution reaction (OER) electrocatalysts. *Angew. Chem., Int. Ed.* **2019**, *58*, 1252–1265.

[44] Anantharaj, S.; Kundu, S.; Noda, S. "The Fe effect": A review unveiling the critical roles of Fe in enhancing OER activity of Ni and Co based catalysts. *Nano Energy* **2021**, *80*, 105514.

[45] Yao, Y. C. *Controllable Synthesis and Atomic Scale Regulation of Noble Metal Catalysts*; Springer: Singapore, 2022.

[46] You, B.; Tang, M. T.; Tsai, C.; Abild-Pedersen, F.; Zheng, X. L.; Li, H. Enhancing electrocatalytic water splitting by strain engineering. *Adv. Mater.* **2019**, *31*, 1807001.

[47] Abascal, E.; Gómez-Coma, L.; Ortiz, I.; Ortiz, A. Global diagnosis of nitrate pollution in groundwater and review of removal technologies. *Sci. Total Environ.* **2022**, *810*, 152233.

[48] Foglar, L.; Briški, F.; Sipos, L.; Vuković, M. High nitrate removal from synthetic wastewater with the mixed bacterial culture. *Bioresource Technol.* **2005**, *96*, 879–888.

[49] Zhou, J.; Wen, M.; Huang, R.; Wu, Q. S.; Luo, Y. X.; Tian, Y. K.; Wei, G. F.; Fu, Y. Q. Regulating active hydrogen adsorbed on grain boundary defects of nano-nickel for boosting ammonia electrosynthesis from nitrate. *Energy Environ. Sci.* **2023**, *16*, 2611–2620.

[50] Katsounaros, I.; Figueiredo, M. C.; Chen, X. T.; Calle-Vallejo, F.; Koper, M. T. M. Structure- and coverage-sensitive mechanism of no reduction on platinum electrodes. *ACS Catal.* **2017**, *7*, 4660–4667.

[51] Hadjiivanov, K.; Avreyska, V.; Klissurski, D.; Marinova, T. Surface species formed after NO adsorption and NO + O_2 coadsorption on ZrO_2 and sulfated ZrO_2: An FTIR spectroscopic study. *Langmuir* **2002**, *18*, 1619–1625.

[52] Fang, J. Y.; Zheng, Q. Z.; Lou, Y. Y.; Zhao, K. M.; Hu, S. N.; Li, G.; Akdim, O.; Huang, X. Y.; Sun, S. G. Ampere-level current density ammonia electrochemical synthesis using CuCo nanosheets simulating nitrite reductase bifunctional nature. *Nat. Commun.* **2022**, *13*, 7899.

[53] Lv, C. D.; Zhong, L. X.; Liu, H. J.; Fang, Z. W.; Yan, C. S.; Chen, M. X.; Kong, Y.; Lee, C.; Liu, D. B.; Li, S. Z. et al. Selective electrocatalytic synthesis of urea with nitrate and carbon dioxide. *Nat. Sustain.* **2021**, *4*, 868–876.

[54] Liu, S. S.; Qian, T.; Wang, M. F.; Ji, H. Q.; Shen, X. W.; Wang, C.; Yan, C. L. Proton-filtering covalent organic frameworks with superior nitrogen penetration flux promote ambient ammonia synthesis. *Nat. Catal.* **2021**, *4*, 322–331.

[55] Yao, Y.; Zhu, S. Q.; Wang, H. J.; Li, H.; Shao, M. H. A spectroscopic study of electrochemical nitrogen and nitrate reduction on rhodium surfaces. *Angew. Chem., Int. Ed.* **2020**, *59*, 10479–10483.

[56] Zhao, R. D.; Yan, Q. Y.; Yu, L. H.; Yan, T.; Zhu, X. Y.; Zhao, Z. Y.; Liu, L.; Xi, J. Y. A Bi-Co corridor construction effectively improving the selectivity of electrocatalytic nitrate reduction toward ammonia by nearly 100%. *Adv. Mater.* **2023**, *35*, 2306633.

[57] Zheng, Q.; Xu, H. Y.; Yao, Y. C.; Dai, J.; Wang, J. X.; Hou, W.; Zhao, L.; Zou, X. Y.; Zhan, G. M.; Wang, R. Z. et al. Cobalt single-atom reverse hydrogen spillover for efficient electrochemical water dissociation and dechlorination. *Angew. Chem., Int. Ed.* **2024**, *63*, e202401386.

[58] Zhang, M. L.; Zhang, Z. D.; Zhang, S. L.; Zhuang, Z. C.; Song, K. P.; Paramaiah, K.; Yi, M. Y.; Huang, H.; Wang, D. S. Efficient electrochemical nitrate reduction to ammonia driven by a few nanometer-confined built-in electric field. *ACS Catal.* **2024**, *14*, 10437–10446.

[59] Hong, Q. L.; Zhou, J.; Zhai, Q. G.; Jiang, Y. C.; Hu, M. C.; Xiao, X.; Li, S. N.; Chen, Y. Cobalt phosphide nanorings towards efficient electrocatalytic nitrate reduction to ammonia. *Chem. Commun.* **2021**, *57*, 11621–11624.

[60] Zhang, Q.; Xiao, W.; Guo, W. H.; Yang, Y. X.; Lei, J. L.; Luo, H. Q.; Li, N. B. Macroporous array induced multiscale modulation at the surface/interface of $Co(OH)_2$/NiMo self-supporting electrode for effective overall water splitting. *Adv. Funct. Mater.* **2021**, *31*, 2102117.

[61] Karamad, M.; Goncalves, T. J.; Jimenez-Villegas, S.; Gates, I. D.; Siahrostami, S. Why copper catalyzes electrochemical reduction of nitrate to ammonia. *Faraday Discuss.* **2023**, *243*, 502–519.

[62] Fan, K.; Xie, W. F.; Li, J. Z.; Sun, Y. N.; Xu, P. C.; Tang, Y.; Li, Z.

H.; Shao, M. F. Active hydrogen boosts electrochemical nitrate reduction to ammonia. *Nat. Commun.* **2022**, *13*, 7958.

[63] Yuan, C. Z.; Jiang, Y. F.; Wang, Z.; Xie, X.; Yang, Z. K.; Yousaf, A. B.; Xu, A. W. Cobalt phosphate nanoparticles decorated with nitrogen-doped carbon layers as highly active and stable electrocatalysts for the oxygen evolution reaction. *J. Mater. Chem. A* **2016**, *4*, 8155–8160.

[64] Zhang, R. Y.; van Straaten, G.; Di Palma, V.; Zafeiropoulos, G.; van de Sanden, M. C. M.; Kessels, W. M. M.; Tsampas, M. N.; Creatore, M. Electrochemical activation of atomic layer-deposited cobalt phosphate electrocatalysts for water oxidation. *ACS Catal.* **2021**, *11*, 2774–2785.

[65] González-Flores, D.; Sánchez, I.; Zaharieva, I.; Klingan, K.; Heidkamp, J.; Chernev, P.; Menezes, P. W.; Driess, M.; Dau, H.; Montero, M. L. Heterogeneous water oxidation: Surface activity versus amorphization activation in cobalt phosphate catalysts. *Angew. Chem., Int. Ed.* **2015**, *54*, 2472–2476.

[66] Odynets, I. V.; Strutynska, N. Y.; Li, J. Z.; Han, W.; Zatovsky, I. V.; Klyui, N. I. $CoO_x(OH)_y$/C nanocomposites *in situ* derived from $Na_4Co_3(PO_4)_2P_2O_7$ as sustainable electrocatalysts for water splitting. *Dalton Trans.* **2018**, *47*, 15703–15713.

[67] Menezes, P. W.; Panda, C.; Walter, C.; Schwarze, M.; Driess, M. A cobalt-based amorphous bifunctional electrocatalysts for water-splitting evolved from a single-source lazulite cobalt phosphate. *Adv. Funct. Mater.* **2019**, *29*, 1808632.

[68] Huang, Y. K.; Song, X. D.; Chen, S. B.; Zhang, J.; Gao, H. Q.; Liao, J. J.; Ge, C. J.; Sun, W. Multi-layer architecture of novel sea urchin-like Co-hopeite to boosting overall alkaline water splitting. *Adv. Mater. Interfaces* **2023**, *10*, 2202349.

[69] Zhao, Y. X.; Shi, R.; Bian, X. A.; Zhou, C.; Zhao, Y. F.; Zhang, S.; Wu, F.; Waterhouse, G. I. N.; Wu, L. Z.; Tung, C. H. et al. Ammonia detection methods in photocatalytic and electrocatalytic experiments: How to improve the reliability of NH_3 production rates. *Adv. Sci.* **2019**, *6*, 1802109.

[70] He, W. H.; Zhang, J.; Dieckhöfer, S.; Varhade, S.; Brix, A. C.; Lielpetere, A.; Seisel, S.; Junqueira, J. R. C.; Schuhmann, W. Splicing the active phases of copper/cobalt-based catalysts achieves high-rate tandem electroreduction of nitrate to ammonia. *Nat. Commun.* **2022**, *13*, 1129.

[71] Notario-Estévez, A.; Kozlov, S. M.; Viñes, F.; Illas, F. Electronic-structure-based material descriptors: (In)dependence on self-interaction and Hartree–Fock exchange. *Chem. Commun.* **2015**, *51*, 5602–5605.

[72] Kresse, G.; Hafner, J. *Ab initio* molecular dynamics for liquid metals. *Phys. Rev. B* **1993**, *47*, 558–561.

[73] Perdew, J. P.; Wang, Y. Accurate and simple analytic representation of the electron-gas correlation energy. *Phys. Rev. B* **1992**, *45*, 13244–13249.

[74] Perdew, J. P.; Burke, K.; Ernzerhof, M. Generalized gradient approximation made simple. *Phys. Rev. Lett.* **1996**, *77*, 3865–3868.